

Lattice-strain field induced by {311} self-interstitial defects in silicon

Paola Alippi*

*Istituto Nazionale per la Fisica della Materia and Dipartimento di Scienza dei Materiali,
Università degli Studi di Milano "Bicocca," via Cozzi 53, 20125 Milano, Italy*

Luciano Colombo

*Istituto Nazionale per la Fisica della Materia
and Dipartimento di Fisica, Università di Cagliari, Cittadella Universitaria, 09042 Monserrato (CA), Italy
(Received 19 November 1999)*

Formation energies and equilibrium configurations of self-interstitial {311} defects in silicon are determined by tight-binding molecular dynamics simulations as well as by the characterization of the lattice-strain field around the defect complex. By means of the determination of the atomic stress distribution, we discuss how the lattice strain may influence the formation mechanisms of the planar {311} structures. A correlation between structural features and electronic properties is also discussed through the analysis of defect-related orbital occupations and inverse participation ratios.

I. INTRODUCTION

The presence of defects in bulk silicon affects its physical properties on a length scale comparable with the typical sample dimensions that experimental techniques can probe and that modern technological applications are in need of. In particular, extended interstitial structures with a well-defined orientation plane have been shown to cause sizeable changes in the properties of the dopant species in silicon.¹ The so-called {311} defects have been observed in electron irradiated as well as ion implanted silicon in a temperature range of $300^\circ\text{C} < T < 800^\circ\text{C}$.^{2,3} Such *rodlike* defects show up in transmission electron microscopy (TEM) observations as interstitial structures elongated in the $\langle 110 \rangle$ direction, having the {311} plane as their habit plane.³ At higher temperature, extended {311} defects evolve into dislocation loops, whereas in *B*-implanted silicon their dissolution during thermal annealing deeply affects the diffusion mechanism of the dopant specie. Experimental investigations¹ have in fact correlated the {311}'s evaporation during the annealing process with the detection of an enhanced diffusion of boron, which penetrates into the bulk of the sample as deep as $0.1\ \mu\text{m}$ with respect to its equilibrium diffusion length. These works have indicated that, at high implantation energy ($\approx 10\ \text{keV}$), the {311}'s are the source of excess self-interstitial defects that in turn contribute to the boron diffusion. Understanding the evolution from small like-defect clusters to *rodlike* structures, and further to planar {311} defects, is thus a key issue for a basic understanding of Si microstructural evolution under bulk processing.

Atomic models of {311} defects have been built up since their discovery,² on the basis of the defect images obtained by TEM experiments.^{3,4} In the attempt to characterize the basic building block of these defects, a given interstitial structure is inserted into the perfect-crystal matrix and the nearby atomic bonds are locally rearranged through educated guesses. In the early work of Tan,² it is pointed out that the introduction of a $\langle 110 \rangle$ chain of interstitial atoms in the perfect diamond structure requires a minimum number of dan-

gling bonds. This is an energetically-favored pathway in bulk Si, as pointed out since the seminal paper by Chadi and Chang.⁵ Thus, following Tan,² all the atomic models of the extended {311} defects have been built up placing several $\langle 110 \rangle$ chains close together on the {311} plane. The insertion of such a basic building block (hereafter referred to as the *I* chain) in the crystal lattice causes the formation of five- and seven-membered atomic rings around the defect core. A particular arrangement of the *I* chains on the {311} plane results in a succession of six-membered rings. This defect structure can be seen as a local precipitate of hexagonal silicon on the {311} plane. From atomistic simulations of TEM images, the presence of eight-membered rings (in the following denoted as *O* rings) separating groups of *I* chains along the $\langle 233 \rangle$ direction, has been first detected by Takeda.³ The *O* ring units are unusual in other kinds of silicon extended defects, such as dislocations faults or grain boundaries, and seem to be peculiar of the {311} structures.

Following those TEM analyses, few theoretical studies⁶⁻⁸ have been presented. Structure stability and growth mechanisms have been discussed mostly in terms of the calculated formation energies of different defect structures, modelled as periodic repetitions of unit blocks containing different arrangements of *I* chains and *O* rings. The introduction of *O* rings was indeed found to be energetically favored both in classical molecular-dynamics simulations⁶ and within tight-binding frameworks.^{7,8}

Our goal is to contribute to the investigation of the {311} planar defects through the study of the lattice stress field around the defect complex. In particular, for reasons that will be clear in the following, we choose to analyze the structures that the work of Kim *et al.*⁸ has shown to be the more stable among those containing the same number of interstitial chains. By comparing the spatial distribution of the stress tensor for different defect geometries we will discuss the dynamical processes involved in the {311}'s formation. The stress tensor distribution can give, in fact, access to the characterization of preferred growth directions of the defect, as well as of an effective range for the capture/emission of in-

terstitial atoms from the defect cores.⁹ Moreover, the transition between confined cluster structures and planar defects could be also discussed by comparing the stress distribution in the two cases.

In the next section (Sec. II), a brief description of the computational framework is given, while in Sec. III we present and discuss our results, analyzing the energetics of formation and the lattice-strain field of the defect structures. A complementary discussion of the electronic properties is also presented, based on calculated inverse participation ratio. Finally, conclusions are drawn in Sec. IV.

II. COMPUTATIONAL SCHEME

We perform tight-binding molecular dynamics¹⁰ (TBMD) simulations within the TB representation for Si developed by Kwon *et al.*¹¹ This representation has been shown to give accurate results for Si bulk properties¹¹ as well as correct formation energies of various native point defects (vacancy and interstitial) when compared to first-principle density functional results (in the local density and the generalized gradient approximation) as well as quantum Monte Carlo calculations.^{12,13} The unit cell used in order to study the {311} defects has orthorhombic symmetry, with the \hat{x}, \hat{y} , and \hat{z} axes parallel, respectively, to the $\langle 0\bar{1}1 \rangle$, $\langle 2\bar{3}\bar{3} \rangle$, and $\langle 311 \rangle$ directions of the diamond lattice. The lengths of the unit cell axes are $L_x = a_0/\sqrt{2}$, $L_y = \sqrt{11}/2a_0$, and $L_z = \sqrt{11}a_0$ (a_0 being the lattice constant of the silicon diamond lattice), resulting in a total number of 44 atoms per unit cell.

A molecular-dynamics study of the {311} defects requires the use of large simulation cells, since periodic boundary conditions as well as constant-volume simulations are being used. In order to avoid artificial interactions between image defect structures, the use of the n_x, n_y, n_z replica of the unit cell along the three directions is mandatory. Since all {311} structures studied here are periodic along the $\langle 0\bar{1}1 \rangle$ direction it is possible to set $n_x = 1$. However, the choice of n_y and n_z forces the size of a typical system to be in the range between ≈ 500 and ≈ 800 atoms. From the analysis of the spatial extension of the atomic stress distribution, we decide in fact to set the spatial separation between end-of-defect atoms of the defect core and of its periodic image along the \hat{y} and \hat{z} direction to be larger than ≈ 12 Å. In order to handle such large cells, we use the linear-scaling order(N)-TBMD method based on the polynomial Fermi operator expansion introduced by Goedecker and Colombo^{10,14} and efficiently implemented in its parallel version on the Cray T3E.

We also mention here that a first qualitative insight onto the stability of the atomic configurations used as starting models of the {311} defect structures is first gained via molecular-dynamics simulations employing the Stillinger-Weber interatomic potential.¹⁵ TBMD simulations within the O(N) scheme are performed on these structures, applying a finite-temperature annealing procedure (up to 600 K). Accurate defect formation energies are finally obtained by means of total energy calculations, performed on the structures annealed and relaxed at zero temperature, with the conventional TBMD scheme based on a full diagonalization of the TB matrix.

In order to investigate the stability of these structures, we

developed a careful analysis of the stress introduced in the crystal by the presence of the {311} defect. The values of the stress tensor $\sigma_{\alpha\beta}$ for a system of N interacting particles with potential energy U can be calculated from the following expression:¹⁶

$$\sigma_{\alpha\beta} = \frac{1}{V} \left\langle \sum_{i=1}^N \left(\frac{p_{i\alpha} p_{i\beta}}{m_i} - r_{i\alpha} \nabla_{i\beta} U \right) \right\rangle_t. \quad (1)$$

Here, $r_{i\alpha}$ and $p_{i\alpha}$ are the α components of, respectively, the position and the momentum vector of the i th atom, while $\langle \dots \rangle_t$ indicates the time average of the quantity within parentheses. We remind here that in our TB picture the potential energy is $U = E_{BS} + U_{rep}$, i.e., the sum of the band-structure energy E_{BS} and the repulsive potential U_{rep} .

To discuss the spatial localization of the strain introduced in the crystal by a defect structure, an atomistic picture of the stress is more useful, in order to identify stress contributions from different regions of the simulation cell. In principle, such atomic decomposition could be derived from Eq. (1) itself, since the latter is a sum of N terms $\sigma_{\alpha\beta}^i$ defined for each particle i . The above equation is valid for any particle-particle interaction that is a differentiable function of the vector positions $\{\mathbf{r}_j\}$: U contains all the many-body interactions and $\sigma_{\alpha\beta}^i$ is thus a function of all particle coordinates. The TB formalism however gives a much simpler formulation of the atomic stress tensor $\sigma_{\alpha\beta}^i$, since E_{BS} and U_{rep} can be written as sum of pairwise terms depending on the distance vector of any atom pair. Thus, the atomic level stress tensor can be written as¹⁶

$$\sigma_{\alpha\beta}^i = \frac{1}{V} \left\langle r_{i\alpha} \sum_{j=1}^N \mathbf{F}_\beta^{(ij)} \right\rangle_t, \quad (2)$$

where $\mathbf{F}^{(ij)} = -\partial U / \partial \mathbf{r}_{ij}$ is the force between atoms i and j and $\mathbf{F}^{(ij)} = \mathbf{F}_{BS}^{(ij)} + \mathbf{F}_{rep}^{(ij)}$.

We remind here that the stress tensor is defined in linear elasticity theory starting from the total force F acting on a given volume V of the material. The relation defining the stress tensor is in fact $F_\alpha = \int (\sum_\beta \partial \sigma_{\alpha\beta} / \partial x_\beta) dV$. The spatial partition of the stress tensor suffers from a gauge problem: in an atomistic picture, this means that two definitions of the atomic stress tensor σ^i that differ by a factor $\Delta \sigma^i$ are equivalent, provided that

$$\sum_\beta \partial \Delta \sigma_{\alpha\beta}^i / \partial x_\beta = 0.$$

We notice however that, even though absolute values of the atomic stress tensor are not meaningful, it is nevertheless correct to consider relative values that are obtained within the same gauge choice. In the next section, in fact, we present our results on the stress field distribution for the {311}'s, obtained comparing the values of $\sigma_{\alpha\beta}^i$ calculated for different defect structures.

III. ENERGETICS AND STRESS ANALYSIS

We have investigated different structures for {311} defects, which are shown in Figs. 1–7. As explained above, the defect unit block is an infinite $\langle 0\bar{1}1 \rangle$ chain of interstitial

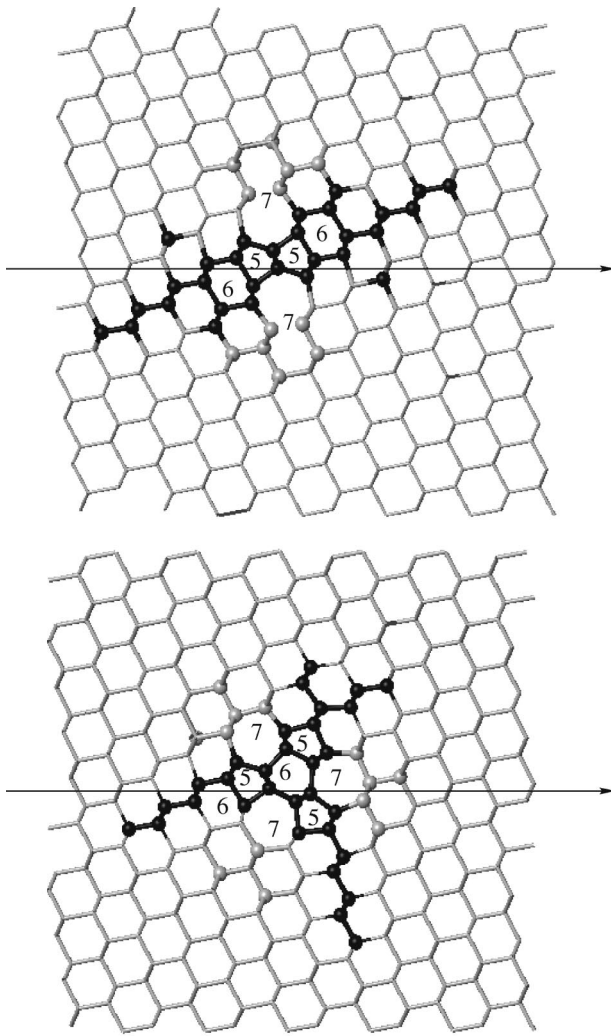


FIG. 1. Relaxed structure (at $T=0$ K) for a single I chain in two possible configurations (see discussion in the text). A color code indicates the value of the atomic stress tensor $\sigma_{\alpha\beta}^i$, calculated from Eq. (1): atoms under positive compressive stress are marked with light gray, while black has been used to indicate atoms under negative tensile stress.

atoms inserted into the crystal lattice. The periodic boundary conditions imposed on the simulation cell allow the investigation of two kinds of defect structures: those in Figs. 1, 2, 4, and 5 have finite size along the $\langle 2\bar{3}\bar{3} \rangle$ direction, while the one in Fig. 6 is infinitely extended in both $\langle 0\bar{1}1 \rangle$ and $\langle 2\bar{3}\bar{3} \rangle$, modelling thus an infinite planar defect. As a further case, Fig. 7 represents an example of configuration often detected in TEM pictures of the $\{311\}$,¹ i.e., two structures having finite size along the $\langle 311 \rangle$ and $\langle 3\bar{1}\bar{1} \rangle$ directions, that cross each other forming a V-shaped defect.⁸

After the insertion of the I chains, the atomic bonds surrounding the interstitial atoms rearrange themselves in order to minimize locally the strains. This is what happens, in fact, after the application of a first thermal annealing cycle (up to 600 K), whose effect is to bring the structure in a local energy minimum. Once it has been stabilized at zero temperature, some of the bonds are rotated in order to investigate slightly different configurations of the defect core that were not obtained at once by the initial thermal annealing proce-

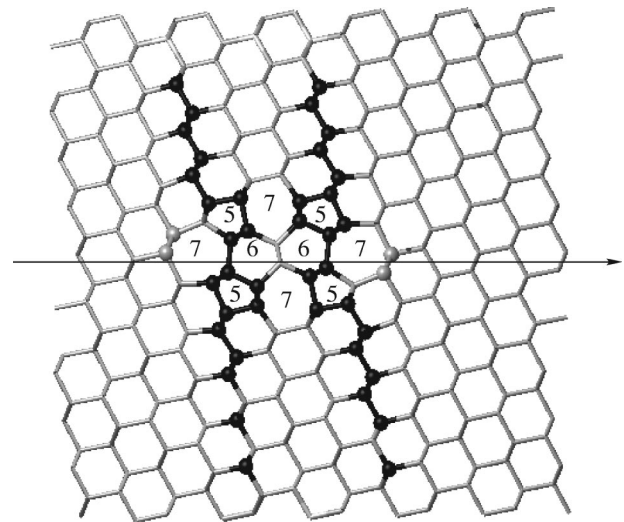


FIG. 2. Relaxed configuration for a $\{311\}$ defect containing a single I chain between two six-membered rings. The same color code of Fig. 1 is used.

dure. A molecular-dynamics run is again performed on these structures, in order to relax them at zero temperature.

Figures 1–7 show $\{311\}$ defects viewed along the $\langle 0\bar{1}1 \rangle$ direction, as the typical defect images obtained by TEM observations. Different n -membered bond rings (i.e., closest paths connecting all neighboring atoms¹⁷) can be recognized and different sequences of them can be identified along the $\langle 2\bar{3}\bar{3} \rangle$ direction (that is marked with a black arrow in the pictures). Table I reports the formation energies of the structures studied, together with a comparison with previous theoretical studies. The formation energies E_f are obtained subtracting the TB total energy E_B of a perfect-crystal unit cell with N_B bulk atoms from the total energy E_{BI} of a defect configuration containing N_I interstitial atoms, as

$$E_f = \left(E_{BI} - \frac{(N_B + N_I)}{N_B} E_B \right), \quad (3)$$

while the formation energies per interstitial E_f^I are calculated simply by E_f/N_I and are listed in Table I. In the table, each structure is identified by the sequence of n -order rings along

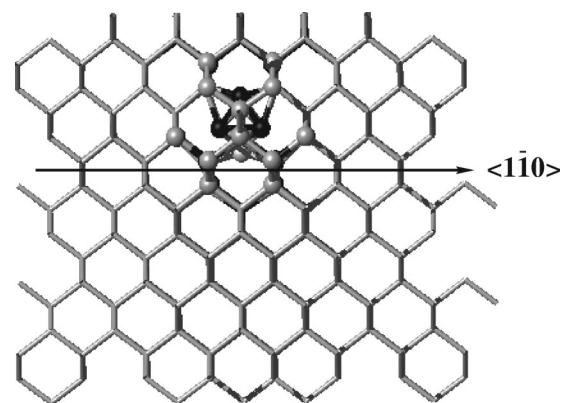


FIG. 3. Atomic stress distribution for a $I11$ cluster in the geometry predicted by the TB calculations of Bongiorno *et al.* (Ref. 18).

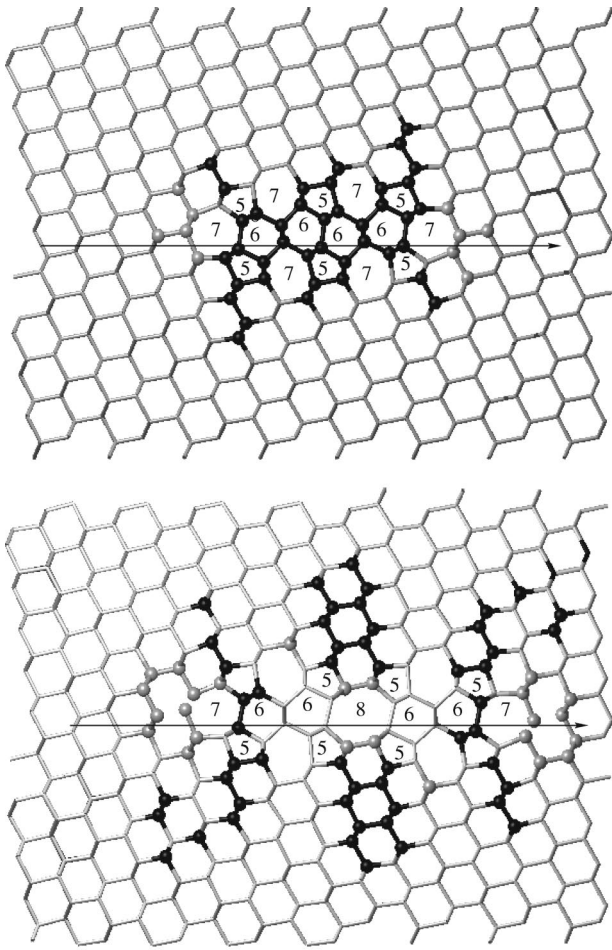


FIG. 4. Relaxed configurations and atomic stress distributions for $\{311\}$ defect containing two I chains. Upper panel: I chains are placed at $L_y/2$ distance. Lower panel: I chains at L_y distance, with the formation of an O ring. The same color code of Fig. 1 is used.

the $\langle 2\bar{3}\bar{3} \rangle$ direction and the number of interstitial that it contains, those numbers being reported in the first two columns.

We start discussing the results for structures containing a single I chain (Figs. 1 and 2). The three configurations present different rearrangement of the atomic bonds around

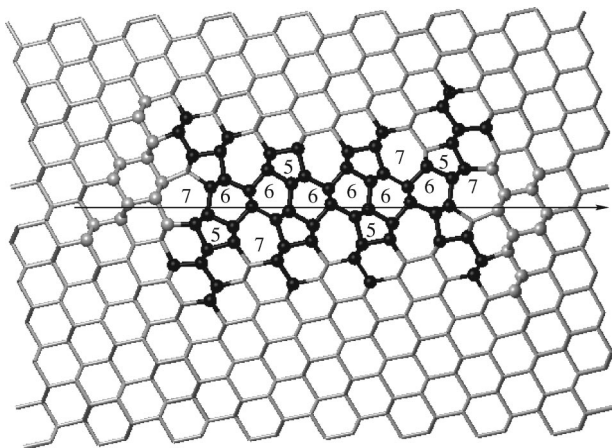


FIG. 5. Relaxed configuration and atomic stress distribution for a $\{311\}$ defect containing three I chains, with a sequence of six-membered rings. The same color code of Fig. 1 is used.

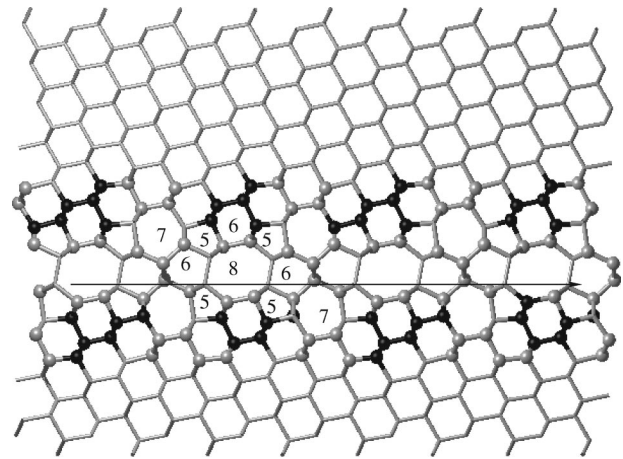


FIG. 6. Relaxed configurations and atomic stress tensor for the periodic $|IO|$ defect. The same color code of Fig. 1 is used.

the I chain, giving the sequences indicated in Table I as $5-I-5$, $5-I-67$, $76-I-67$. We see that the formation energies per interstitial of these defect configurations are different, with the last two being degenerate at 1.6 eV. In agreement with previous studies,^{7,8} we find that these values are in all cases lower than for the most stable self-interstitial defect: the calculated E_f^I are in fact in the range $\approx 1.6-2.05$ eV, compared to a formation energy of 3.2–3.9 eV for the dumbbell structure, as given by first-principle calculations and also by the present TB model.¹² This indicates that clustering of interstitial atoms forming an infinitely long $\langle 0\bar{1}1 \rangle$ chain is favored as compared to separate isolated interstitial atoms. With respect to the work of Kim *et al.*,⁸ we find, in general, formation energies that are lower by about 0.2 eV, although the TB representation adopted in both works is the same. We think this is due to the present more careful relaxation procedure: a thermal annealing procedure has been chosen in order to bring the structures to their relaxed atomic ground state, whereas the steepest-descent method was used in the work of Kim *et al.*⁸

We further calculate the atomic stress tensor according to Eq. (2) for each structure, and show in Figs. 1–7 the results for the hydrostatic component, namely, $\sigma_h = 1/3 \text{Tr } \sigma_{\alpha\beta}$.

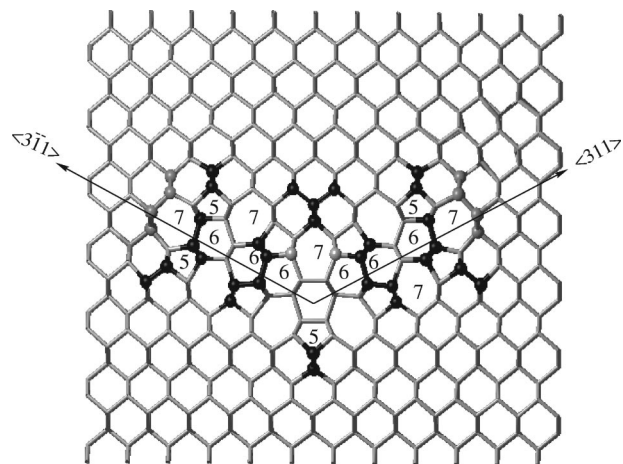


FIG. 7. Relaxed configuration for the V-shaped defect. The same color code of Fig. 1 is used.

TABLE I. Formation-energies per interstitial atom, E_f^I (in eV), for the $\{311\}$ defect structures considered in this work. The first two columns report the succession of n -membered rings along the $\langle 233 \rangle$ direction and the number of I chains of each structure.

	N_{I-c}	E_f^I (eV)
5- I -5	1	2.05 (2.2)
5- I -67	1	1.58 (1.8)
76- I -67	1	1.60 (1.8)
76- I -66- I -67	2	1.21 (1.5)
76- I -686- I -67	2	2.01 (1.6)
76- I -6- I -6- I -67	3	1.13 (1.3)
IO	1	1.35 (1.68)
V shaped	4	1.86 (1.3)

We set the zero level of the stress at 10^{-4} eV/Å³ atoms with σ_h below this threshold are not shown by circles in Figs. 1–7, while those under compressive and tensile stress are colored, respectively, in light gray and black.

Comparing the structures in the upper panel of Fig. 1 with that in Fig. 2, we notice first of all that the stress tensor has different spatial distributions, even though the values of E_f^I differ only by few tenths of eV's. In the upper panel of Fig. 1 it is evident that tensile stress extends along the $[001]$ plane crossing the I chain, while atoms just below and above the I chain are under compressive stress. However, if the sequence of n membered rings along the $\langle 2\bar{3}\bar{3} \rangle$ direction is I -67 (as in the lower panel of Figs. 1 and 2), atoms at the $\langle 2\bar{3}\bar{3} \rangle$ end of the defect core are under compressive stress, while tensile stress extends now in the $[010]$ direction perpendicular to the defect plane.

The structure in Fig. 2 has been assumed⁸ as the building block of the extended $\{311\}$ defect. It is energetically stable, as indicated by the values of E_f^I and it stabilizes locally an hexagonal Si structure: the insertion of the I chain leads, in fact, to the formation of two coplanar hexagonal rings lying on the $\langle 0\bar{1}1 \rangle$ plane (the 6- I -6 sequence). The stress analysis shows that the atoms of the I chains shared by two hexagonal rings are under zero stress, as a consequence of the hexagonal structure of this particular defect core.

In a previous theoretical work¹⁸ the energetics and the geometries of small I clusters containing up to 11 atoms have been studied within the same TB picture adopted here. Values of the formation energy per interstitial are lower than those obtained for a finite $\langle 0\bar{1}1 \rangle$ chain containing the same number of interstitial atoms.^{8,18} In Fig. 3, we show the relaxed configuration for a cluster of 11 interstitial atoms obtained by Bongiorno *et al.*¹⁸ This defect structure is elongated in the $\langle 110 \rangle$ direction and has $E_f^I = 2.27$ eV, larger than the corresponding value obtained for the infinite I chain of Fig. 2 (1.6 eV). Comparison of these E_f^I values may suggest that, in the initial stage of the growth, the leading mechanism for defects nucleation is not the I chain formation, but that more compact and smaller clusters are favored. In this respect, it is useful to compare the stress distributions for the infinite I chains of Figs. 1 and 2 with the one calculated for the elongated I cluster in Fig. 3, in order to discuss the possible transition from finite-dimension structures to the extended ones. We notice how the stress in Fig. 3 is very lo-

calized on the atoms belonging to the cluster. This behavior is very different from the much wider spatial distribution of the stress for the I chain (Fig. 2). The latter involves, in fact, a more extended structural relaxation of the lattice. According to these results it can be argued that, for a limited number of interstitial atoms, small cluster structures elongated in the $\langle 110 \rangle$ direction are energetically preferred and introduce very localized lattice distortions. The stress distributions in Figs. 1 and 2 suggest also that the subsequent formation of the I chain, the building block of the $\{311\}$ defect, is driven by the energetic balance in which the energy cost of spreading the lattice distortion in a larger region of space is compensated by the local stabilization of a tiny hexagonal phase of silicon.

The stress analysis has been carried out also for configurations containing two I chains. These are obtained introducing a new I chain to the relaxed structure of Fig. 2 and performing a thermal annealing cycle. Following Kim *et al.*,⁸ we set the distance between the two I chains along the $\langle 2\bar{3}\bar{3} \rangle$ direction to $L_y/2$ and L_y (upper and lower panel of Fig. 4). In the latter case, the relaxed configuration presents the formation of an eight-membered ring between the two I chains, as in the lower panel of Fig. 4. In accordance with previous work,⁸ we find, in fact, that the O rings are stable when I chains are separated by a distance equal to L_y . The calculated formation energies per interstitial are 1.21 eV (structure in upper panel) and 2.01 eV (lower panel structure).

The color code shows that the atoms belonging to the defect cores are under tensile stress. As already discussed for Fig. 2, atoms belonging to the seven-membered rings and lying at the $\langle 2\bar{3}\bar{3} \rangle$ ends of the defect core are under compressive stress. Comparing the two panels in Fig. 4, we see that the presence of an O ring between two I chains introduces a new feature in the stress distribution: atoms belonging to the I chains are under almost zero stress, and tensile stress extends on the planes perpendicular to the $\{311\}$ plane and crossing the O ring. We calculated also the bond-angle distortions around the defect: we found that the seven- and eight-membered rings introduce a much wider distortion with respect to the perfect crystal than five-membered rings do. The build up of compressive stress around the seven- and eight-membered rings, in spite of their smaller atomic density with respect to the perfect crystal, can be thus interpreted only by bond-bending force mechanism.

For a further comparison, we show in Fig. 5 a defect configuration containing three I chains separated by a $L_y/2$ distance, where the sequence of I chains and six-order rings (6- I -6) builds up a more extended hexagonal structure. From Figs. 4 and 5 we conclude that when several 6- I -6 unit blocks are packed together along the $\langle 2\bar{3}\bar{3} \rangle$ direction, as in Fig. 5, a high degree of tensile stress is localized on the atomic planes surrounding the defect. We remind, in fact, that the hexagonal structure in the core of the defect is strained, since it does not lie on its natural plane but on the $\{311\}$. The stress distribution of Fig. 4 suggests that this tensile stress can be relieved when a less compact structure is formed, as it is the case when the eight-membered ring is introduced in the structure between two adjacent I chains. This result agrees with the indications coming from atomic simulations of TEM pictures: configurations with subsequent

I chains along the $\langle 2\bar{3}\bar{3} \rangle$ direction are not favored, and the relative occurrence of I chains deduced from experiments is approximately 67%.⁷

In Fig. 6, a different $\{311\}$ structure is presented, infinitely extended along both \hat{x} and \hat{y} axes. The unit block that is periodically repeated consists of a single I chain and an O ring. This structure has a formation energy per interstitial equal to 1.35 eV. As is evident from the picture, few atomic planes above and below the $\{311\}$ plane are under stress. The stress distribution has different features with respect to those observed in all previous finite configurations, i.e., the presence of compressive stress on the $\langle 2\bar{3}\bar{3} \rangle$ end-of-defect atoms and of tensile stress extending along directions perpendicular to the $\{311\}$ plane. Hence, these features seem to be due to the presence of the $\langle 2\bar{3}\bar{3} \rangle$ edges and disappear for structure that are also periodic in the $\langle 2\bar{3}\bar{3} \rangle$ direction. The atomic decomposition of the stress is here similar to the one in the lower panel of Fig. 4, confirming that the introduction of the eight-membered ring into the hexagonal defect core built up by the I chains does indeed alter the lattice strain field.

Finally, Fig. 7 shows a V -shaped defect, i.e., the crossing of two defect structure like that in Fig. 2, lying along the $\langle 2\bar{3}\bar{3} \rangle$ and $\langle 2\bar{3}\bar{3} \rangle$ directions. Here again compressive stress shows up at the edge atoms and tensile stress on the $\langle 010 \rangle$ planes; moreover, the stress distribution shows that the tensile stress is also localized on atoms inside the kink.

In order to further substantiate the above structural analysis, we have also investigated the electronic structure of the $\{311\}$ defect configurations, analyzing the degree of localization of the electronic states on individual atoms. The inverse participation ratio¹⁹ $I(\Psi_n)$ has been taken as a measure of the spatial localization of the electronic state Ψ_n . $I(\Psi_n)$ is defined from the tight-binding coefficients a_{li}^n , projections of Ψ_n on the basis function $\phi_l(\mathbf{R}_i)$ localized on the i atom, as

$$I(\Psi_n) = N \frac{\sum_{il} (a_{li}^n)^4}{\left[\sum_{il} (a_{li}^n)^2 \right]^2}. \quad (4)$$

In the limiting cases of extended ($a_{li}^n = 1/N$) or localized ($a_{li}^n = a \delta_{ik}$) electronic states $I(\Psi_n)$ assumes the values of 1 and N , respectively.

We consider first the 6- I -6 structure of Fig. 2, where we noticed first of all that there is no appearance of electronic states in the gap. The building block of the defect has in fact all Si atoms fourfold coordinated: since no atom with higher/lower coordination is introduced in the crystal lattice, no dangling bonds are to be expected. The situation would be of course different for a finite I chain. For what concerns the inverse participation ratio calculations, the degree of localization of the electronic states is very small; all IPR values are in fact below ≈ 10 . We stress here that the same feature is found for all other defect structures (Figs. 4–7).

IV. CONCLUSIONS

In summary, we have investigated the stress field around chosen atomic models of silicon $\{311\}$ defects, relaxed at zero temperature by means of TBMD calculations. We have shown that a local rearrangement of the atomic bonds around the defect complex may influence the stress distribution, suggesting a way to discuss the formation mechanism of the $\{311\}$ defects. The structural analysis is consistent with the electronic structure where no gap state-related features are found, in accordance with the fourfold coordination character of all investigated structures.

ACKNOWLEDGMENTS

We acknowledge computational support on the CRAY-T3E computer at CINECA by INFN under the Parallel Computing Initiative ‘‘From point to extended self-interstitials in silicon: a TBMD investigation.’’ We also acknowledge financial support by MURST under the project ‘‘Nanostrutture indotte da bombardamento ionico’’ (COFIN-98). We thank Dr. Jeongnim Kim for helpful suggestions.

*Author to whom correspondence should be addressed. Electronic address: paola.alippi@mater.unimib.it

¹D.J. Eaglesham, P.A. Stolk, H.-J. Gossmann, and J.M. Poate, Appl. Phys. Lett. **65**, 2305 (1994); A. Agarwal, T.E. Haynes, D.J. Eaglesham, H.-J. Gossmann, D.C. Jacobson, J.M. Poate, and Y.E. Erokhin, *ibid.* **70**, 3332 (1997).

²I.G. Salisbury and M.H. Loretto, Philos. Mag. A **39**, 317 (1979); T.Y. Tan, *ibid.* **44**, 101 (1981).

³Seiji Takeda, Jpn. J. Appl. Phys., Part 2 **30**, L639 (1991).

⁴A. Parisini and A. Bourret, Philos. Mag. A **67**, 605 (1993).

⁵D.J. Chadi and K.J. Chang, Phys. Rev. B **38**, 1523 (1988).

⁶M. Kohyama and S. Takeda, Phys. Rev. B **46**, 12 305 (1992).

⁷M. Kohyama and S. Takeda, Phys. Rev. B **51**, 13 111 (1995).

⁸J. Kim, J.W. Wilkins, F.S. Khan, and A. Canning, Phys. Rev. B **55**, 16 186 (1997); H. Kohno, T. Mabuchi, S. Takeda, M. Kohyama, and M. Tanaka, Phys. Rev. B **58**, 10 388 (1998).

⁹A. Bongiorno and L. Colombo, Phys. Rev. B **57**, 8767 (1998).

¹⁰L. Colombo, in *Annual Reviews of Computational Physics*, edited

by D. Stauffer (World Scientific, Singapore, 1996), Vol. IV, p. 147.

¹¹I. Kwon, R. Biswas, C.Z. Wang, K.M. Ho, and C.M. Soukoulis, Phys. Rev. B **49**, 7242 (1994).

¹²M. Tang, L. Colombo, J. Zhu, and T. Diaz de la Rubia, Phys. Rev. B **55**, 14 279 (1997).

¹³W.-K. Leung, R.J. Needs, G. Rajagopal, S. Itoh, and S. Ihara, Phys. Rev. Lett. **83**, 2351 (1999).

¹⁴S. Goedecker and L. Colombo, Phys. Rev. Lett. **73**, 122 (1994).

¹⁵F.H. Stillinger and T.A. Weber, Phys. Rev. B **31**, 5262 (1985).

¹⁶G. De Sandre, L. Colombo, and C. Bottani, Phys. Rev. B **54**, 11 857 (1996).

¹⁷D.S. Franzblau, Phys. Rev. Lett. **44**, 4925 (1991).

¹⁸L. Colombo, Physica B **272-274**, 458 (1999); A. Bongiorno, L. Colombo, F. Cargnoni, C. Gatti, and M. Rosati, Europhys. Lett. **50**, 608 (2000).

¹⁹J. Dong and D.A. Drabold, Phys. Rev. Lett. **80**, 1928 (1998).